DRAFT
CMS Paper

The content of this note is intended for CMS internal use and distribution only

Alignment of the CMS Muon System
with Cosmic-Ray and Beam-Halo Muons

The CMS Collaboration

Abstract

The CMS muon system has been aligned using cosmic-ray muons collected in 2008 and beam-halo muons from the 2008 LHC circulating beam tests. After alignment, the resolution of the most sensitive coordinate is 80 microns for the relative positions of superlayers in the same barrel chamber and 270 microns for the relative positions of endcap chambers in the same ring structure. The resolution on the position of the central barrel chambers relative to the tracker is comprised between two extreme estimates, 200 and 700 microns, provided by two complementary studies. With minor modifications, the alignment procedures can be applied using muons from LHC collisions, leading to additional significant improvements.

1 Introduction

The primary goal of the Compact Muon Solenoid (CMS) experiment [1] is to explore particle physics at the TeV energy scale exploiting the proton-proton collisions delivered by the Large Hadron Collider (LHC) [2]. The CMS experiment features a large muon tracking system for identifying muons and reconstructing their momenta. As with all tracking systems, the momentum resolution of reconstructed tracks depends in part on the alignment of detector components in space: three translational and three rotational degrees of freedom for each component. The alignment procedure provides corrections to the relationships between local detector-bound coordinate frames and a single, global frame for all CMS tracking systems.

The muon system consists of hundreds of independent tracking chambers mounted within the CMS magnetic field return yoke. Three technologies are employed: Drift Tube (DT) chambers on the five modular wheels of the barrel section, Cathode Strip Chambers (CSC) on the six endcap disks (illustrated in Figs. 1 and 2) and Resistive Plate Chambers (RPC) throughout. The DTs and CSCs are sufficiently precise to contribute to the momentum resolution of high-momentum muons (several hundred GeV/c) assuming that these chambers are well-aligned relative to the CMS tracker, a one-meter radius silicon strip and pixel detector. Between the tracker and the muon system are electromagnetic and hadronic calorimeters (ECAL and HCAL, respectively) for particle identification and energy measurement, as well as the solenoid coil for producing an operating magnetic field strength of 3.8 T in which to measure charged-particle momenta (all shown in Fig. 1).

The CMS collaboration is developing multiple techniques to align the DT and CSC chambers and their internal layers. Photogrammetry and in-situ measurement devices [3] provide real-time monitoring of potential chamber movements on short timescales and measurements of degrees of freedom to which tracks are only weakly sensitive. Track-based alignment, the subject of this paper, optimizes component positions for a given set of tracks, directly relating the active elements of the detectors traversed by the charged particles in a shared coordinate frame. Methods using tracks are employed both to align nearby components relative to one another and to align all muon chambers relative to the tracker.

A challenge to track-based alignment in the CMS muon system is the presence of large quantities of material between the chambers. As a central design feature of the detector, 20–60 cm layers of steel are sandwiched between the chambers to concentrate the magnetic field and absorb beam-produced hadrons. Consequently, uncertainties in track trajectories become significant as muons propagate through the material, making it necessary to develop alignment procedures that are insensitive to scattering, even though typical deviations in the muon trajectories (3–8 mm) are large compared to the intrinsic spatial resolution (100–300 μm). Two types of approaches are presented in this paper: the relative alignment of nearby structures, which avoids extrapolation of tracks through material but does not relate distant coordinate frames to each other, and the alignment using tracks reconstructed in the tracker, which allows for a more sophisticated treatment of propagation effects by simplifying the interdependence of alignment parameters.

This paper begins with a brief overview of the geometry of the muon system and conventions to be used thereafter (Section 2), followed by presentations of three alignment procedures:

(a) internal alignment of layers within DT chambers using a combination of locally fitted track segments and survey measurements (Section 3);

(b) alignment of groups of overlapping CSC chambers relative to one another, using only
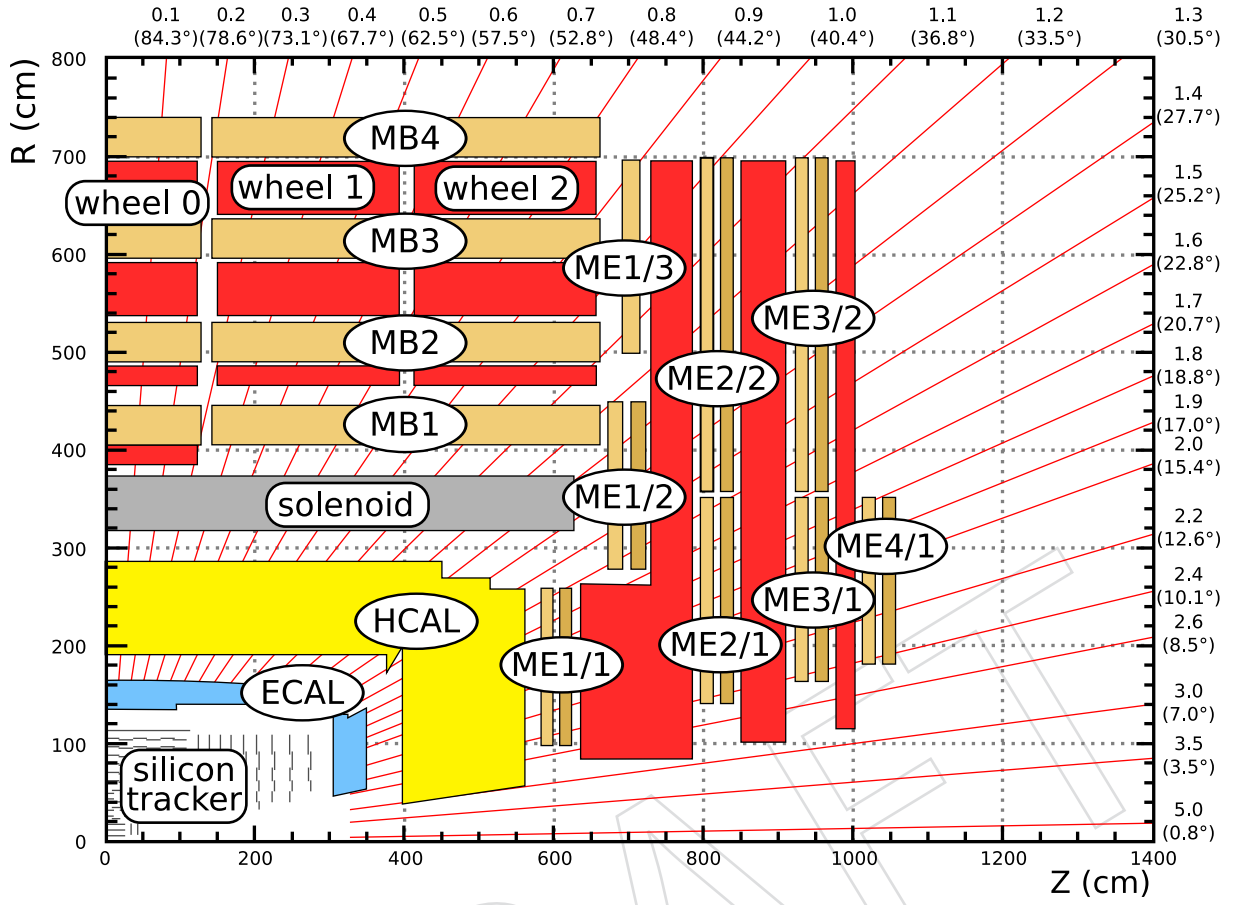
Figure 1: Quarter-view of CMS with labeled muon barrel (MB) and endcap (ME) stations. The steel yoke is represented by darkly shaded (red) blocks between the muon chambers. Pseudo-rapidities and polar angles are indicated on the top and right edges of the diagram.
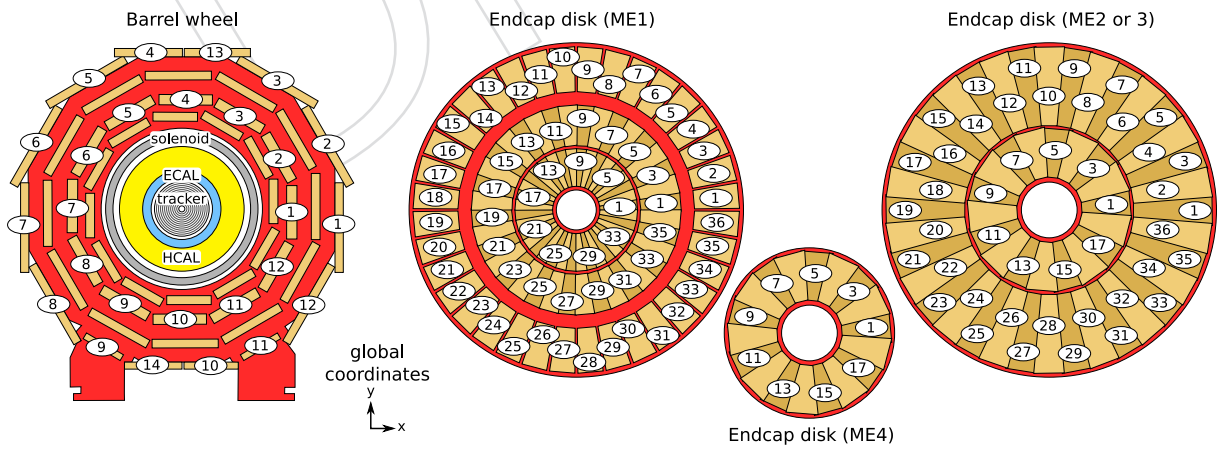

Figure 2: Transverse slices of CMS: the central barrel wheel and representative endcap disks, indicating the numbering of the DT azimuthal sectors in the barrel and the CSC chamber numbers in the endcaps.

46 locally fitted track segments (Section 4);

47 (c) alignment of each chamber relative to the tracker, using the tracks from the tracker, prop-
48 agated to the muon system with a detailed map of the magnetic field and material distri-
49 bution of CMS (Section 5).

50 Procedure (c), above, completes the alignment, relating all local coordinate frames to a shared
51 frame. Its performance is greatly improved by supplying internally aligned chambers from
52 procedure (a), such that only rigid-body transformations of whole chambers need to be consid-
53 ered. Procedures (b) and (c) both align CSC chambers relative to one another, but in different
54 ways: (b) does not need many tracks, only about 1000 per chamber, to achieve high precision,
55 and (c) additionally links the chambers to the tracker.

56 With the first LHC collisions, groups of CSCs will be interaligned using (b) and these rigid-
57 body groups will be aligned relative to the tracker with (c). As more data become available,
58 comparisons of results from (b) and (c) yield highly sensitive tests of systematic errors in (c).

59 Although the ideal tracks for these procedures are muons from LHC collisions, this paper fo-
60 cuses on application of the procedures using currently available data, namely cosmic rays (a
61 and c) and beam-halo muons from circulating LHC beam tests in September 2008 (b). In par-
62 ticular, (c) requires a magnetic field to select high-quality, high-momentum muons and concur-
63 rent operation of the tracker and muon systems. The CMS Collaboration conducted a month-
64 long data-taking exercise known as the Cosmic Run At Four Tesla (CRAFT) during October–
65 November 2008, with the goal of commissioning the experiment for extended operation [4].
66 With all installed detector systems participating, CMS recorded 270 million cosmic-ray trig-
67 gered events with the solenoid at its nominal axial field strength of 3.8 T. Due to geometric
68 limitations imposed by the primarily vertical distribution of cosmic rays underground, (c) is
69 performed with only a subset of DT chambers using CRAFT data, though the procedure will
70 apply similarly to CSC chambers, once a large sample of inclined tracks becomes available.

71 The formalism and results of each procedure are presented together. Details of the data transfer
72 and the computing model which were used to implement these procedures are described in
73 Ref. [5].

2 Geometry of the Muon System and Definitions

75 Muon chambers are independent, modular track detectors, each containing 6–12 measurement
76 layers, sufficient to determine the position and direction of a passing muon from the intersec-
77 tions of its trajectory with the layer planes ("hits"). The DT layers are oriented nearly perpen-
78 dicular to lines radially projected from the beamline, and CSC layers are perpendicular to lines
79 parallel with the beamline. Hits are initially expressed in a local coordinate frame (x, y, z) de-
80 fined by the layers: $z = 0$ is the plane of the layer and x is the more precisely measured (or the
81 only measured) of the two plane coordinates. On CSC layers, the most precise measurement
82 is given by cathode strips, which fan radially from the beamline [6]. Defining "local $r\phi$" as the
83 curvilinear coordinate orthogonal to the strips at all points, x and local $r\phi$ coincide only at the
84 center of each CSC layer.

85 A semi-local coordinate system for the entire chamber is defined with x, y, and z axes nominally
86 parallel to the layers' axes, but with a single origin. Within this common frame, the positions
87 of hits from different layers can be related to each other and combined by a linear fit into
88 segments with position $(\bar{x}, \bar{y})$ and direction $(\frac{dx}{dz}, \frac{dy}{dz})$. The nominal x direction of every chamber
89 is perpendicular to the beamline and radial projections from the beamline.
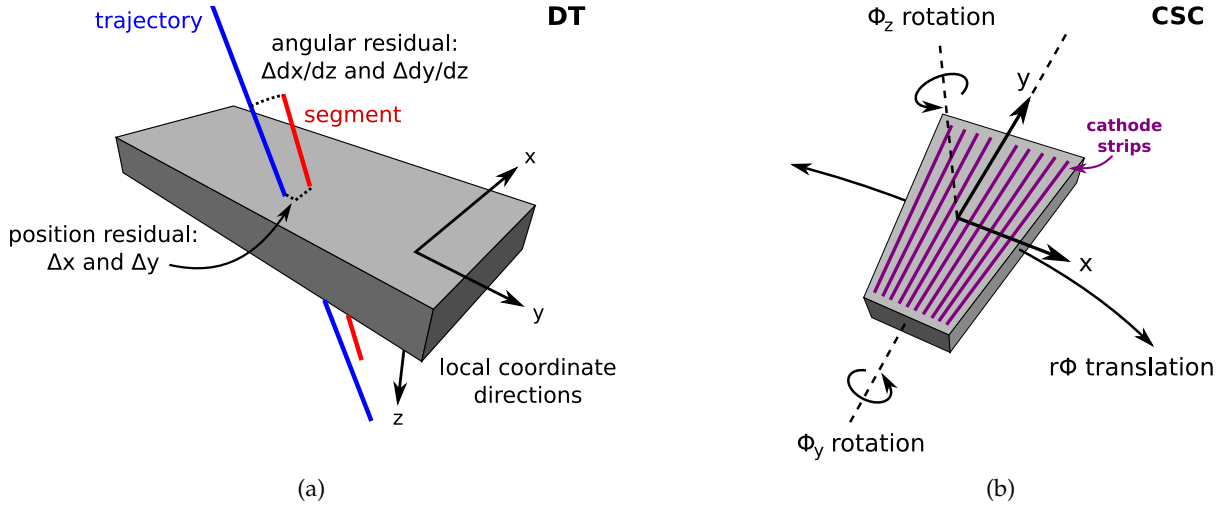
Figure 3: (a) Coordinates and residuals for a DT chamber. (b) Coordinates and alignment parameters for a CSC chamber.

90 Residuals are differences between the predicted particle trajectories and the muon chamber
91 data. Residuals can have as few as one component, from layers that measure only one dimen-
92 sion in the measurement plane, and as many as four components, Δx, Δy, $\Delta \frac{\mathrm{d}x}{\mathrm{d}z}$, $\Delta \frac{\mathrm{d}y}{\mathrm{d}z}$, from linear
93 fits to all residuals in a chamber, as illustrated in Fig. 3(a).

94 To compare chamber positions to each other and to the position of the tracker, consider global
95 coordinates (X, Y, Z) with the origin at the symmetry center of CMS, Z axis directed anti-
96 clockwise along the beamline, Y upward, and X horizontally toward the center of the LHC
97 ring. Local coordinate systems are related to one another through an Alignment Integration
98 Frame (AIF) that only approximates these global coordinates. It is not necessary to tightly con-
99 trol the definition of the AIF, as global translations and rotations of the whole system do not
100 affect any physics measurements. Specific coordinate frames, at intermediate levels between
101 layers and chambers and between chambers and global, are introduced in this paper as needed.

102 Corrections to positions and orientations of the layers and chambers are denoted as δ_x, δ_y,
103 δ_z, δ_{ϕ_x}, δ_{ϕ_y}, and δ_{ϕ_z}, with x, y, and z expressed in local coordinates of the layer or chamber,
104 and ϕ_x, ϕ_y, and ϕ_z as rotations around the corresponding axis; alignment corrections are small
105 enough, $\mathcal{O}(\mathrm{mrad})$, to approximately commute. For CSC chambers, $\Delta(r\phi)$, $\Delta \frac{\mathrm{d}(r\phi)}{\mathrm{d}z}$, and $\delta_{r\phi}$ are
106 more appropriate than Δx, $\Delta \frac{\mathrm{d}x}{\mathrm{d}z}$, and δ_x, respectively, to take advantage of the precision of the
107 cathode strips. The most sensitive CSC alignment parameters are illustrated in Fig. 3(b).

108 DT layers are grouped into four-layer "superlayers," each of which measures one coordinate.
109 Most DT chambers contain three superlayers, and the middle one, superlayer 2, is oriented a
110 $90°$ angle with respect to superlayers 1 and 3 to measure y positions in the chamber coordinate
111 frame. DT chambers farthest from the interaction point (MB4 in Fig. 1) contain only super-
112 layers 1 and 3, and are therefore insensitive to y and $\frac{\mathrm{d}y}{\mathrm{d}z}$. CSC chambers contain six identical
113 layers.

114 Chambers are grouped into "stations" by their distance from the interaction region, named
115 MB1–MB4 in the barrel and ME$\pm 1/1$, $\pm 1/2$, $\pm 1/3$, $\pm 2/1$, $\pm 2/2$, $\pm 3/1$, $\pm 3/2$, and $\pm 4/1$ in the
116 endcaps, labeled in Fig. 1. Azimuthal positions are called "sectors" in the barrel and simply
117 "chamber number" in the endcaps, and these are labeled in Fig. 2.

3 Internal Alignment of DT Chambers

The layers and superlayers of DT chambers are aligned and analyzed in two steps. First, all layers in the chamber are aligned using a general Millepede algorithm [7], simultaneously optimizing alignment parameters and segment parameters, subject to constraints from a survey performed during construction. In the second step, the alignment of superlayers 1 and 3 are checked by fitting segments in each superlayer separately and measuring alignment errors from deviations between pairs of superlayer segments.

3.1 Layer Alignment

Measured trajectories within a single chamber do not suffer from uncertainties due to scattering in the steel between chambers. Segments, determined from linear fits to hits in one chamber only, are therefore used to determine the alignment of layers inside the chamber. The segment parameters depend on the layer alignment parameters within the chamber, so both must be resolved in a combined fit.

Without external constraints, the combined fit does not have a unique optimum, as it is insensitive to global distortions of the chamber. Consider a shear of the chamber that translates each layer in x by an amount proportional to its z position and an equal shear of all segment angles: this new geometry has exactly the same residuals as the unsheared geometry.

It is therefore necessary to add external survey measurements to constrain the fit; these are taken from two sources: (1) measurements of the wire end-pins taken during superlayer construction, and (2) photographs of reflective targets on the exterior of the superlayer ("photogrammetry"), taken during chamber construction. The averages of wire positions for all wires in each layer provide measurements of the x positions of the layers: RMS deviations from design geometry are 100 μm with 30–40 μm uncertainties. RMS deviations for the photogrammetry measurements are 200 μm in x and y, 500 μm in z, and 150 μrad in ϕ_x, ϕ_y, and ϕ_z.

The alignment of a tracking system subject to survey constraints can be expressed as the minimum of an objective function with terms derived from both tracks and survey. The objective function is

$$\chi^2 = \sum_i^{\text{layers}} \sum_j^{\text{tracks}} \left(\Delta \vec{x}_{ij} - A_j \cdot \vec{\delta}_i - B_i \cdot \delta \vec{p}_j \right)^T (\sigma_{\text{hit}}{}^2)_{ij}^{-1} \left(\Delta \vec{x}_{ij} - A_j \cdot \vec{\delta}_i - B_i \cdot \delta \vec{p}_j \right)$$
$$+ \sum_i^{\text{layers}} \sum_k^{\text{targets}} \left(\Delta \vec{\xi}_k - C_{ik} \cdot \vec{\delta}_i \right)^T (\sigma_{\text{survey}}{}^2)_k^{-1} \left(\Delta \vec{\xi}_k - C_{ik} \cdot \vec{\delta}_i \right) + \lambda \left| \sum_i^{\text{layers}} \vec{\delta}_i \right|^2 \quad , \quad (1)$$

where

- $\Delta \vec{x}_{ij}$ is the residual on layer i from track j (one-dimensional and in layer coordinates for the layer alignment case);

- $\vec{\delta}_i = (\delta_x, \delta_y, \delta_z, \delta_{\phi_x}, \delta_{\phi_y}, \delta_{\phi_z})$ is a vector of alignment corrections for layer i;

- $A_j = \begin{pmatrix} 1 & 0 & -\frac{dx}{dz}_j & -y_j \frac{dx}{dz}_j & x_j \frac{dx}{dz}_j & -y_j \end{pmatrix}$ is a 1×6 matrix transforming alignment parameter errors to residuals, dependent on the layer intersection (x_j, y_j) and entrance angle $\frac{dx}{dz}_j$ of track j;

- $\delta \vec{p}_j$ is a vector of corrections to the segment parameters;

- B_i is a matrix transforming variation of segment parameters into residuals on layer i (including a projection to the measured direction in the layer coordinate system);

152   • $(\sigma_{\mathrm{hit}}{}^2)_{ij}^{-1}$ is the inverse of the covariance matrix of the uncertainty in the hit on layer
153   i, track j (single-valued in the layer alignment case);

154   • $\Delta\vec{\zeta}_k$ is the difference between the nominal and measured position of survey target k;

155   • C_{ik} is a matrix transforming alignment errors in layer i to corrections in the position
156   of survey target k;

157   • $(\sigma_{\mathrm{survey}}{}^2)_k^{-1}$ is the inverse of the covariance matrix of measurement k;

158   • $\lambda \left| \sum_i \vec{\delta}_i \right|^2$ is a Lagrange multiplier to inhibit translations and rotations of the chamber.

159 Segments are modeled as straight lines because the magnetic field is negligible inside the DT
160 chambers. Survey targets from wire measurements are one-dimensional (the other two coor-
161 dinates are given zero inverse uncertainties in $(\sigma_{\mathrm{survey}}{}^2)_k^{-1}$) and photogrammetry targets are
162 included as individual survey constraints. Wire measurements apply only to relative positions
163 of layers within their parent superlayer, and photogrammetry constraints apply to all layers in
164 a superlayer as a group. This is expressed in $C_{ik} \cdot \vec{\delta}_i$ with terms such as $\vec{\delta}_i - [\vec{\delta}_1 + \vec{\delta}_2 + \vec{\delta}_3 + \vec{\delta}_4]/4$
165 to constrain layer i in a superlayer consisting of layers 1–4. Errors in survey measurements are
166 assumed to be uncorrelated.

167 The χ^2 is quadratic in its parameters, so it is solved by the matrix inversion method. All layers
168 were aligned in δ_x, δ_{ϕ_x}, δ_{ϕ_y}, and δ_{ϕ_z}, using about 20 000 cosmic ray tracks per chamber. The RMS
169 of the corrections is 116 μm, 58 μrad, 63 μrad, and 49 μrad, respectively, and will be studied in
170 more detail in the next section.

171 ## 3.2   Test of Superlayer Alignment

172 To cross-check the alignment results in superlayers 1 and 3, the track-based data are compared
173 with an independent set of photogrammetry measurements. The four hits in each superlayer
174 define a superlayer segment with a one-dimensional position and slope, and segments from
175 different superlayers must match at a common plane. Segment residuals, Δx_{S}, are the mis-
176 match of these superlayer segments, and are sensitive to relative positions of the superlayers
177 as well as their internal layer alignment parameters.

Segment residuals can be used to align superlayers 1 and 3 relative to one another without
needing external constraints. The first term in Eq. (1) becomes

$$\chi_{\mathrm{S}}{}^2 = \sum_j^{\mathrm{tracks}} \left[\Delta x_{\mathrm{S}j} - \left(\begin{matrix} 1 & -\dfrac{\mathrm{d}x}{\mathrm{d}z}\Big|_j & x_j\dfrac{\mathrm{d}x}{\mathrm{d}z}\Big|_j \end{matrix} \right) \cdot \left(\begin{matrix} \delta_{x_{\mathrm{S}}} \\ \delta_{z_{\mathrm{S}}} \\ \delta_{\phi_{y_{\mathrm{S}}}} \end{matrix} \right) \right]^2 \frac{1}{(\sigma_{\Delta x_{\mathrm{S}}})_j^2} \quad , \qquad (2)$$

178 with no explicit dependence on track parameter corrections $\delta\vec{p}_j$. The minimization of Eq. (2)
179 has a unique solution in $\delta_{x_{\mathrm{S}}}$, $\delta_{z_{\mathrm{S}}}$, and $\delta_{\phi_{y_{\mathrm{S}}}}$. It is not susceptible to shear, for example, because the
180 slopes of the segments are fixed by the layers in each superlayer. Access to additional alignment
181 parameters would require knowledge of y and $\frac{\mathrm{d}y}{\mathrm{d}z}$ which are not available in superlayers 1 and
182 3. The position of superlayer 2 cannot be determined in this way because it is the only y-
183 measuring detector in a DT chamber.

184 To check the partially survey-based layer alignment from Section 3.1, segment residuals before
185 and after layer alignment are plotted in Fig. 4(a). Each entry in the histogram is the mean of the
186 Δx_{S} distribution for a single chamber. After layer alignment, segment positions and angles are
187 more consistent between superlayers 1 and 3, leading to better matching at the common plane.

188 To verify the photogrammetry superlayer positions, $\delta_{x_{\mathrm{S}}}$, $\delta_{z_{\mathrm{S}}}$, and $\delta_{\phi_{y_{\mathrm{S}}}}$ from a minimization of
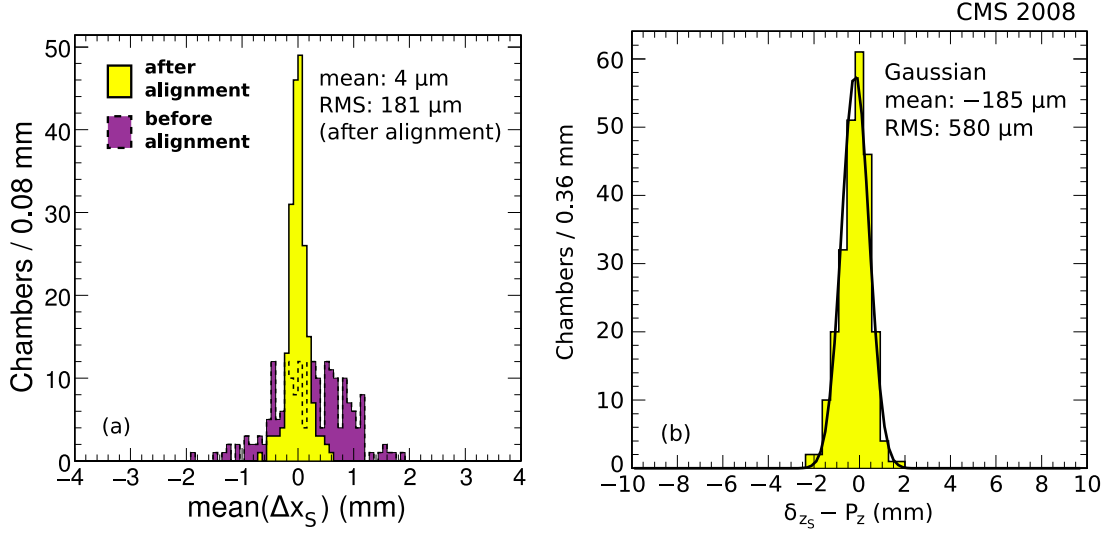
Figure 4: (a) Distribution of means of DT segment residuals for all chambers, before alignment presented in a dark/dashed histogram and after alignment in a light histogram. (b) Difference in z of superlayers as measured by tracks (δ_{z_S}) and photogrammetry (P_z).

Eq. (2) are directly compared with the photogrammetry measurements P_x, P_z, and P_{ϕ_y} of the relative superlayer positions. Figure 4(b) presents differences between the δ_{z_S} and P_z for each chamber. Typical values of δ_{z_S} are 1–1.5 mm due to a glue layer not included in the design geometry, and they agree with P_z on a per-chamber basis with 580 μm accuracy. Agreement of δ_{x_S} and $\delta_{\phi_{y_S}}$ with P_x and P_{ϕ_y}, respectively, have 80 μm and 50 μrad accuracy. The segment measurements were applied to correct the internal geometry of the chambers.

4   Alignment of CSC Chambers in Rings

The CSC chambers in the muon endcaps were designed to overlap slightly along the edges of the sensitive area, such that muons passing through the narrow "overlap regions" would be observed by both of the neighboring chambers. This allows for a high-precision relative alignment of neighbors, and the relative measurements can be propagated around each ring of mutually overlapping chambers (illustrated in Fig. 2). All endcap rings are internally connected in this way except ME±1/3.

Although CSC chamber alignment using overlap tracks and alignment with tracks from the tracker (described in the next section) both determine the relative positions of CSC chambers, the overlap method has two advantages: (1) it achieves high precision with a small number of tracks, and (2) it is less prone to potential systematic errors in tracking. Since the two methods use different datasets in different ways, comparison between them can be used to diagnose systematic errors in tracks from the tracker or in their propagation to the muon endcaps. The disadvantage of the overlap alignment method is that it does not relate the ring coordinate frame to the AIF. A second alignment step is therefore necessary to align the whole ring as a rigid body relative to tracks from the tracker.

This section begins with a mathematical derivation of the algorithm, which is an analytic solution of Eq. (1) without external constraints, followed by an analysis of results from a Monte Carlo (MC) simulation and LHC single-beam tests. Cosmic ray results are not presented because the procedure requires forward-pointing tracks with approximate azimuthal symmetry.

4.1 Ring Alignment Algorithm

The basic strategy of CSC ring alignment is to fit segments from the same muon in each of the overlapping chambers independently and require them to match in position and slope for all chambers in the ring simultaneously. Segment parameters $\overline{r\phi}$ and $\frac{\mathrm{d}(r\phi)}{\mathrm{d}z}$ are computed using only cathode strips (the high-precision $r\phi$ coordinate), in a coordinate frame shared by pairs of chambers with $z = 0$ being the plane of symmetry between them. The curvature added to the segments by parameterizing them with a curvilinear coordinate is negligible. Chambers are labeled by indices i ranging from 1 to N ($N = 18$ or 36, depending on the ring), with the convention that $N + 1$ refers to chamber 1.

The general alignment objective function (see Eq. (1) for definitions) could be applied here, removing survey constraints and considering each track to consist of two "hits" with two components each: $\overline{r\phi}^i_j$ and $\frac{\mathrm{d}(r\phi)}{\mathrm{d}z}{}^i_j$. However, the geometry of this alignment case allows for simplifications which make the solution analytic. Overlap tracks only connect neighboring chambers, i and $i + 1$, in such a way that residuals $\Delta(r\phi)^i_j = \overline{(r\phi)}^i_j - \overline{(r\phi)}^{i+1}_j$ and $\Delta\frac{\mathrm{d}(r\phi)}{\mathrm{d}z}{}^i_j = \frac{\mathrm{d}(r\phi)}{\mathrm{d}z}{}^i_j - \frac{\mathrm{d}(r\phi)}{\mathrm{d}z}{}^{i+1}_j$ constrain $A_j \cdot \left(\vec{\delta}^i - \vec{\delta}^{i+1}\right)$. Minimization of terms with the form

$$\begin{pmatrix} \Delta(r\phi)^i_j \\ \Delta\frac{\mathrm{d}(r\phi)}{\mathrm{d}z}{}^i_j \end{pmatrix} - A_j \cdot \left(\vec{\delta}^i - \vec{\delta}^{i+1}\right) \tag{3}$$

is functionally equivalent to Eq. (1) with $B_i \cdot \delta\vec{p}_j$ explicitly evaluated.

The overlap region is narrow in x and $\frac{\mathrm{d}x}{\mathrm{d}z}$ but wide in y, so three alignment parameters, $\delta_{r\phi}$, δ_{ϕ_y}, δ_{ϕ_z} can be accessed from these data (illustrated in Fig. 3(b)). The expression $A_j \cdot \left(\vec{\delta}^i - \vec{\delta}^{i+1}\right)$ expands to

$$\begin{pmatrix} 1 & 0 & -y_j \\ 0 & 1 & 0 \end{pmatrix} \begin{pmatrix} \delta^i_{r\phi} - \delta^{i+1}_{r\phi} \\ \delta^i_{\phi_y} - \delta^{i+1}_{\phi_y} \\ \delta^i_{\phi_z} - \delta^{i+1}_{\phi_z} \end{pmatrix}. \tag{4}$$

Furthermore, correlations between $\delta^i_{\phi_y} - \delta^{i+1}_{\phi_y}$ and $\delta^i_{r\phi} - \delta^{i+1}_{r\phi}$ can be replaced with an order dependence. Rotating chambers (with segments following their orientation) to make segments parallel (ϕ_y alignment) would change their intercepts at $z = 0$, but translating chambers to make segments continuous at $z = 0$ ($r\phi$ alignment) would not change their slopes. If ϕ_y is aligned first and all segments are refitted, recomputing all residuals with the new geometry, a subsequent alignment of $r\phi$ (and ϕ_z) does not disturb the ϕ_y minimization. Therefore, two objective functions, $\chi_1{}^2$ and $\chi_2{}^2$, can be minimized separately as long as $\chi_1{}^2$ is optimized first, and the derived geometry is used to calculate quantities in $\chi_2{}^2$.

Putting all of this together,

$$\chi_1{}^2 = \sum_i^{\text{chambers}} \sum_j^{\text{tracks}} \left[\Delta\frac{\mathrm{d}(r\phi)}{\mathrm{d}z}{}^i_j - \left(\delta^i_{\phi_y} - \delta^{i+1}_{\phi_y}\right)\right]^2 \frac{1}{(\sigma_{\frac{\mathrm{d}(r\phi)}{\mathrm{d}z}}{}^2)^i_j} \tag{5}$$

$$\chi_2{}^2 = \sum_i^{\text{chambers}} \sum_j^{\text{tracks}} \left[\Delta(r\phi)^i_j - \left(\delta^i_{r\phi} - \delta^{i+1}_{r\phi}\right) + y_j\left(\delta^i_{\phi_z} - \delta^{i+1}_{\phi_z}\right)\right]^2 \frac{1}{(\sigma_{r\phi}{}^2)^i_j},$$

where $(\sigma_{\frac{\mathrm{d}(r\phi)}{\mathrm{d}z}}{}^2)^i_j$ and $(\sigma_{r\phi}{}^2)^i_j$ are one-parameter errors in the residuals.

The sum over tracks in $\chi_1{}^2$ can be recognized as a weighted mean and the sum over tracks in $\chi_2{}^2$ as a linear fit of $\Delta(r\phi)_j^i$ versus y. Evaluating them (and introducing m, a, and b as functions returning the weighted mean, y intercept, and slope versus y of a given dataset, respectively), the objective functions can be replaced with

$$
\begin{aligned}
\chi_1'{}^2 &= \sum_i^{\text{chambers}} \left[m\!\left(\left\{\Delta\tfrac{\mathrm{d}(r\phi)}{\mathrm{d}z}{}^i_j\right\}\right) - \left(\delta_{\phi_y}^i - \delta_{\phi_y}^{i+1}\right) \right]^2 \\[2mm]
\chi_{2a}'{}^2 &= \sum_i^{\text{chambers}} \left[a\!\left(\left\{\Delta(r\phi)_j^i, y_j\right\}\right) - \left(\delta_{r\phi}^i - \delta_{r\phi}^{i+1}\right) \right]^2 \\[2mm]
\chi_{2b}'{}^2 &= \sum_i^{\text{chambers}} \left[b\!\left(\left\{\Delta(r\phi)_j^i, y_j\right\}\right) - \left(\delta_{\phi_z}^i - \delta_{\phi_z}^{i+1}\right) \right]^2 \quad,
\end{aligned}
\tag{6}
$$

where $\chi_1'{}^2$ differs from $\chi_1{}^2$ by a constant factor and $\chi_{2a}'{}^2 + \chi_{2b}'{}^2$ differs from $\chi_2{}^2$ by a constant factor. To avoid rotations and twists of the whole ring, Lagrange multiplier $(\sum_i \delta_{\phi_y}^i / N)^2$ is added to $\chi_1'{}^2$, $(\sum_i \delta_{r\phi}^i / N)^2$ is added to $\chi_{2a}'{}^2$, and $(\sum_i \delta_{\phi_z}^i / N)^2$ is added to $\chi_{2b}'{}^2$, which favor solutions with minimal average corrections. Each of the three minimization problems has the same analytic solution, found by setting the derivatives of the objective function to zero and inverting the resulting $N \times N$ matrix of constants. This alignment method is applicable to any tracking system composed of a ring of pairwise overlapping detectors.

The method also enables three internal cross-checks; the following must be consistent with zero: $\sum_i a(\{\Delta(r\phi)_j^i, y_j\})$, $\sum_i b(\{\Delta(r\phi)_j^i, y_j\})$, and $\sum_i m(\{\Delta\tfrac{\mathrm{d}(r\phi)}{\mathrm{d}z}{}^i_j\})$. These closure tests are not sensitive to misalignments, but they determine whether the residuals are consistent with a closed loop. All three closure tests were found to be consistent with zero in these studies.

4.2 Monte Carlo Study

The procedure was applied to beam-halo events generated by Monte Carlo (based on a simulation described in Ref. [8]). The simulation has approximately the same number of events as the 2008 LHC dataset (33 000 tracks passing through the overlap regions of CSCs), but a different azimuthal and radial distribution. The distribution of beam-halo events is difficult to predict for a new accelerator, and in fact changed frequently during the first circulating beam tests. Since the alignment uncertainties are statistics-limited and the population of tracks in each chamber is only approximately the same as in data, the simulation provides only a rough guide for what to expect from the data.

From an initially misaligned detector, the procedure aligned δ_{ϕ_y} with 1.04 mrad accuracy (initially 2 mrad), $\delta_{r\phi}$ with 230 μm (initially 1000 μm), and δ_{ϕ_z} with 0.25 mrad (initially 1 mrad), determined from the RMS of differences between the aligned positions and the true positions of the chambers.

The second step, aligning the internally aligned rings relative to the tracker, was studied with a sample of simulated muons from proton collisions. It was found that 280 μm ring position accuracy in the X-Y plane can be achieved with 10 pb^{-1} of collisions. This second step cannot be applied with beam-halo muons because they generally do not cross both the muon chambers and the tracker.

4.3 Alignment Results

In September 2008, protons circulated in the LHC, producing beam-halo muons captured by CMS. The majority of the beam-halo data were collected from one 9-minute fill of the anti-
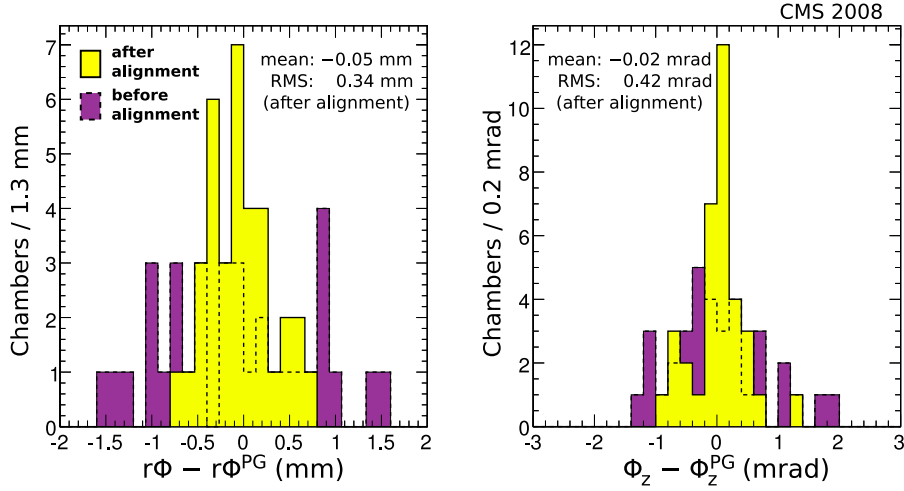
Figure 5: Difference between CSC positions and their photogrammetry measurements. Dark/dashed histograms are before alignment and light histograms are after alignment.

271 clockwise beam. More beam-halo muons illuminated the inner rings of the negative endcap
272 because they tend to follow trajectories close to the beam-line and the anti-clockwise beam tra-
273 verses CMS from the negative side. All chambers in ME$-2/1$ and ME$-3/1$ were operational,
274 so these chambers were used to test the procedure.

275 Application of the alignment algorithm narrows the RMS of the $\Delta(r\phi)$ distribution from 1.42
276 to 0.98 mm. For comparison, the $\Delta(r\phi)$ distribution of the aligned simulation has an RMS of
277 1.12 mm.

278 To independently verify the results, they can be compared with photogrammetry measure-
279 ments. The resolution in the positions of photogrammetry targets is 300 μm [9], which trans-
280 lates into resolutions of 210 μm and 0.23 mrad for $\delta_{r\phi}$ and δ_{ϕ_z} respectively. Photogrammetry
281 measurements cannot determine δ_{ϕ_y} because the targets lie near the y axis of the chambers.

282 Figure 5 shows the difference between chamber coordinates and photogrammetry ($r\phi^{\text{PG}}$ and
283 ϕ_z^{PG}), before and after alignment. The RMS of these distributions after alignment, which
284 are convolutions of photogrammetry errors and errors in the track-based measurements, are
285 340 μm and 0.42 mrad in $\delta_{r\phi}$ and δ_{ϕ_z} respectively. Subtracting the photogrammetry errors in
286 quadrature, one can conclude that the track-based measurement has approximately 270 μm
287 and 0.35 mrad uncertainties, in rough agreement with the prediction from simulation. In the
288 absence of systematic uncertainties, several hours of similar beam-halo conditions would be
289 sufficient to reduce the alignment error below the 170–200 μm intrinsic hit uncertainty for these
290 chambers [6].

5   Alignment of DT Chambers in a Global Coordinate System

292 The muon alignment procedures presented in previous sections arrange layers and sets of
293 chambers in self-consistent coordinate frames, but do not relate those frames to the other sub-
294 systems of CMS, in particular the tracker. In this section, a method is described to align muon
295 chambers relative to the tracker by propagating the tracker tracks to the muon chambers. The
296 method is equally applicable to DTs and CSCs, but cosmic rays only provide large numbers of
297 tracks in the central region of the barrel.

298 Muons encounter significant scattering material between every two stations. With measure-

ments expressed as chamber residuals (Δx, Δy, $\Delta \frac{dx}{dz}$, $\Delta \frac{dy}{dz}$), this means there is a large component of random error in the trajectory between each measurement and the next. The residuals are therefore broadened beyond what would be expected from the intrinsic resolutions of the hits, but alignment information can be derived from the peak positions of those distributions.

In principle, muon chamber hits could be used in the track fits to narrow the distributions of residuals and improve the statistical precision of the alignment results. Including those hits biases the tracks, coupling track parameters and alignment parameters, thereby coupling alignment parameters of different chambers with each other. This coupling can be resolved by matrix inversion [7] or by reducing the weight of the muon chamber hits and iterating [10], but the structure of the probability distribution from scattering complicates these methods. Moreover, sufficient statistical precision can be achieved without muon chamber hits in the track fits (or equivalently, muon chamber hits with negligible weight in the fit).

This section describes muon chamber alignment using tracks determined purely by the tracker. Because the track parameters are not a function of the muon chamber positions, there is no mutual dependency to resolve, nor are the alignment parameters of different chambers coupled. However, the resulting chamber positions depend on the alignment of the tracker [11]: optimized muon chamber residuals does not guarantee that the combined tracker-muon system is globally undistorted. The first subsection below describes the algorithm with a discussion of propagation effects. Section 5.2 presents a Monte Carlo study of the procedure, and alignment results are presented in Sections 5.3 (residuals), 5.4 (cross-check), and 5.5 (momentum measurements). An alternative algorithm is under development to align muon chambers using matrix inversion; this is briefly described in Section 5.6.

5.1 The Reference-Target Algorithm

The "reference-target" algorithm divides the tracking volume into two regions: a "reference" (the tracker), in which normal track-fitting is performed, and a "target" (the muon chambers), in which unbiased residuals are computed from the propagated tracks. The simplicity this affords in the correlation matrix of alignment parameters allows more emphasis to be placed on the study of propagation effects.

The shape of the residuals distribution is fitted to a parameterized Ansatz function using an unbinned maximum likelihood method, rather than minimizing an objective function with a quadratic form like Eq. (1). This can be seen as a generalization of the standard method, because quadratic terms such as $(\Delta x_{ij} - A_j \cdot \vec{\delta}_i)^2 / (\sigma_{\text{hit}}^2)_{ij}$ are the logarithm of Gaussian likelihoods. Substituting a non-Gaussian Ansatz motivated by physical processes in track propagation introduces non-linearity to the derivative of the objective function which cannot be solved by matrix inversion. The non-linear minimization package MINUIT is used instead [12].

5.1.1 Propagation Effects

Residuals from propagated tracks can be affected by the following effects:

- misalignment (distributed as a δ-function in x, y, $\frac{dx}{dz}$, $\frac{dy}{dz}$ because it is strictly geometric);
- intrinsic hit resolution (negligible);
- statistical uncertainty in the fitted track parameters (Gaussian);
- hard Coulomb scattering off of nuclei (which has non-Gaussian tails);
- multiple Coulomb scattering (Gaussian in the limit of many interactions);
- background from pattern-recognition errors and noisy channels (non-Gaussian);

- systematic errors in magnetic field map and material budget for average energy loss (proportional to q/p_T and $q/|\vec{p}|^2$, respectively, where q, p_T, and $|\vec{p}|$ are the charge, transverse momentum, and magnitude of the momentum of the muon);

- systematic bias in the track source distribution (a function of the path of the track through the reference volume).

All but the last two effects are included in the Ansatz. The main non-Gaussian contribution is from events in which the muon interacts with a small number of nuclei, such that the distribution of deflections does not fully reach the Gaussian limit of the central limit theorem. There is no sharp distinction between single and multiple scattering, but it is sufficient to model the combined effect with a function having a Gaussian core and large tails, such as the tails of a Cauchy-Lorentz distribution. A smaller non-Gaussian contribution from pattern-recognition errors and noisy channels is also absorbed into the tails. The primary significance of the tails is to increase the likelihood of highly non-Gaussian residuals, and therefore stabilize the determination of the peak.

A magnetic field map resulting from detailed modeling and CRAFT data analysis [13] was used in this alignment, but the result is additionally verified by performing it separately with positively charged muons, negatively charged muons, and averaging the two. Magnetic field errors add contributions to residuals which are antisymmetric in charge, as do material budget errors because muons can only lose energy on average, and this deflects them in the direction of their curvature. Any charge-dependent effects from magnetic field map or material budget errors would cancel in the average. The RMS of differences with respect to not applying this averaging procedure are 100 μm in δ_x and 0.07 mrad in δ_{ϕ_y}, the two parameters most affected by magnetic field. These differences are small compared with other uncertainties.

The possibility of systematic bias in the track source has been addressed in the context of tracker alignment [14, 15] as weak modes in the procedure and has been studied in Ref. [11] for the tracker description used here. Any unresolved global distortions in the tracker would be extended to the muon system as well, though tracks would be guaranteed to match segments in the momentum range of the algorithm's application. The goal at this stage is to align muon chambers to the positions projected by the current best knowledge of the shape of the tracker.

5.1.2   The Alignment Ansatz Function

Misalignment offsets the peak of the residuals distribution, centering $(\Delta x, \Delta y, \Delta\frac{\mathrm{d}x}{\mathrm{d}z}, \Delta\frac{\mathrm{d}y}{\mathrm{d}z})$ at the values

$$
\begin{pmatrix} \Delta x_0 \\[1.2em] \Delta y_0 \\[1.2em] \Delta\dfrac{\mathrm{d}x}{\mathrm{d}z}_0 \\[1.2em] \Delta\dfrac{\mathrm{d}y}{\mathrm{d}z}_0 \end{pmatrix}
=
\begin{pmatrix}
1 & 0 & -\dfrac{\mathrm{d}x}{\mathrm{d}z} & -y\dfrac{\mathrm{d}x}{\mathrm{d}z} & x\dfrac{\mathrm{d}x}{\mathrm{d}z} & -y \\[1.2em]
0 & 1 & -\dfrac{\mathrm{d}y}{\mathrm{d}z} & -y\dfrac{\mathrm{d}y}{\mathrm{d}z} & x\dfrac{\mathrm{d}y}{\mathrm{d}z} & x \\[1.2em]
0 & 0 & 0 & -\dfrac{\mathrm{d}x}{\mathrm{d}z}\dfrac{\mathrm{d}y}{\mathrm{d}z} & 1+\left(\dfrac{\mathrm{d}x}{\mathrm{d}z}\right)^2 & -\dfrac{\mathrm{d}y}{\mathrm{d}z} \\[1.2em]
0 & 0 & 0 & -1-\left(\dfrac{\mathrm{d}y}{\mathrm{d}z}\right)^2 & \dfrac{\mathrm{d}x}{\mathrm{d}z}\dfrac{\mathrm{d}y}{\mathrm{d}z} & \dfrac{\mathrm{d}x}{\mathrm{d}z}
\end{pmatrix}
\begin{pmatrix} \delta_x \\[1.2em] \delta_y \\[1.2em] \delta_z \\[1.2em] \delta_{\phi_x} \\[1.2em] \delta_{\phi_y} \\[1.2em] \delta_{\phi_z} \end{pmatrix}
, \quad (7)
$$

where (x, y) represents the coordinates of the track intersection with the chamber and $\left(\frac{\mathrm{d}x}{\mathrm{d}z}, \frac{\mathrm{d}y}{\mathrm{d}z}\right)$ the entrance angle. The above matrix is an extension of Eq. (17) in Ref. [10] to include angular residuals $\Delta\frac{\mathrm{d}x}{\mathrm{d}z}$ and $\Delta\frac{\mathrm{d}y}{\mathrm{d}z}$, significantly increasing sensitivity to δ_{ϕ_y} and δ_{ϕ_x}, respectively.

A Voigt distribution, or convolution of a Gaussian with a Cauchy-Lorentzian, is used to model the Gaussian core with large tails. The function

$$f(t; t_0, \sigma, \Gamma) = \int_{-\infty}^{\infty} \frac{1}{\pi} \frac{\Gamma/2}{(t - s - t_0)^2 + (\Gamma/2)^2} \times \frac{1}{\sqrt{2\pi}\sigma} \exp\left(\frac{-s^2}{2\sigma^2}\right) ds \quad , \tag{8}$$

has one variable t with three parameters t_0, σ, and Γ. Close to the peak, the distribution is approximately Gaussian (because $\Gamma \ll \sigma$, typically by a factor of 10), and far from the peak, the distribution is approximately $1/t^2$.

The fit function for the four-dimensional residuals distribution is built from a product of four Voigt distributions. To account for correlations between Δx and $\Delta\frac{dx}{dz}$, and between Δy and $\Delta\frac{dy}{dz}$, parameters $\alpha_{\Delta x}$ and $\alpha_{\Delta y}$ express linear dependences between them in the fit function, and are allowed to float freely in the alignment fit. The correlation is simply due to the fact that an error in the track direction $\Delta\frac{dx}{dz}$ introduced at a distance L upstream of the chamber causes a $\Delta x \approx L\Delta\frac{dx}{dz}$ error in position.

Without explicitly substituting the alignment parameters, the full fit function is

$$F\Big(\Delta x, \Delta y, \Delta\tfrac{dx}{dz}, \Delta\tfrac{dy}{dz};$$

$$\Delta x_0, \Delta y_0, \Delta\frac{dx}{dz}_0, \Delta\frac{dy}{dz}_0, \sigma_{\Delta x}, \sigma_{\Delta y}, \sigma_{\Delta\frac{dx}{dz}}, \sigma_{\Delta\frac{dy}{dz}}, \Gamma_{\Delta x}, \Gamma_{\Delta y}, \Gamma_{\Delta\frac{dx}{dz}}, \Gamma_{\Delta\frac{dy}{dz}}, \alpha_{\Delta x}, \alpha_{\Delta y} \Big) =$$

$$f\Big(\Delta x; (\Delta x_0 + \alpha_{\Delta x}\Delta\tfrac{dx}{dz}), \sigma_{\Delta x}, \Gamma_{\Delta x} \Big) \times f\Big(\Delta\tfrac{dx}{dz}; \Delta\tfrac{dx}{dz}_0, \sigma_{\Delta\frac{dx}{dz}}, \Gamma_{\Delta\frac{dx}{dz}} \Big)$$

$$f\Big(\Delta y; (\Delta y_0 + \alpha_{\Delta y}\Delta\tfrac{dy}{dz}), \sigma_{\Delta y}, \Gamma_{\Delta y} \Big) \times f\Big(\Delta\tfrac{dy}{dz}; \Delta\tfrac{dy}{dz}_0, \sigma_{\Delta\frac{dy}{dz}}, \Gamma_{\Delta\frac{dy}{dz}} \Big) \quad . \tag{9}$$

Substituting Δx_0, Δy_0, $\Delta\frac{dx}{dz}_0$, $\Delta\frac{dy}{dz}_0$ from Eq. (7) introduces the track position and entrance angle as four new variables and the alignment parameters as six new parameters. All parameter values and estimates of their uncertainties are evaluated by MINUIT, seeded by the truncated mean and RMS of each distribution. An example fit is shown in Fig. 6.

The alignment fit is weighted to reduce the influence of poorly formed segments. The quality of a segment is quantified by χ^2/ndf, rather than uncertainties in its parameters, so segments in the alignment fit are weighted by $w_i = (\text{ndf}/\chi^2)_i / \sum_{i'} (\text{ndf}/\chi^2)_{i'}$ of the segment fits. The objective function minimized by the alignment is $\chi^2 = \sum_i w_i \log F_i$ where F_i is given by Eq. (9) for each segment i. To avoid domination of the fit by a few of the most linear segments, which are not necessarily from the best-determined tracks (unscattered muons), segments with the largest 1% of weights have been excluded.

To resolve unmodeled non-linearities in the residuals, the procedure is applied twice, taking the output of the first iteration as an initial geometry for the second. No subsequent improvements are observed in a third iteration or beyond.

5.1.3 Configuration for Alignment with Cosmic-Ray Muons

The vertical distribution of cosmic rays underground imposed geometric restrictions on the set of chambers that could be aligned with this algorithm. Only barrel wheels -1, 0, $+1$, excluding horizontal sectors 1 and 7 (see Fig. 2), recorded a sufficient number of muons that also crossed the barrel of the tracker to perform an alignment. In addition, the fits for four nearly horizontal
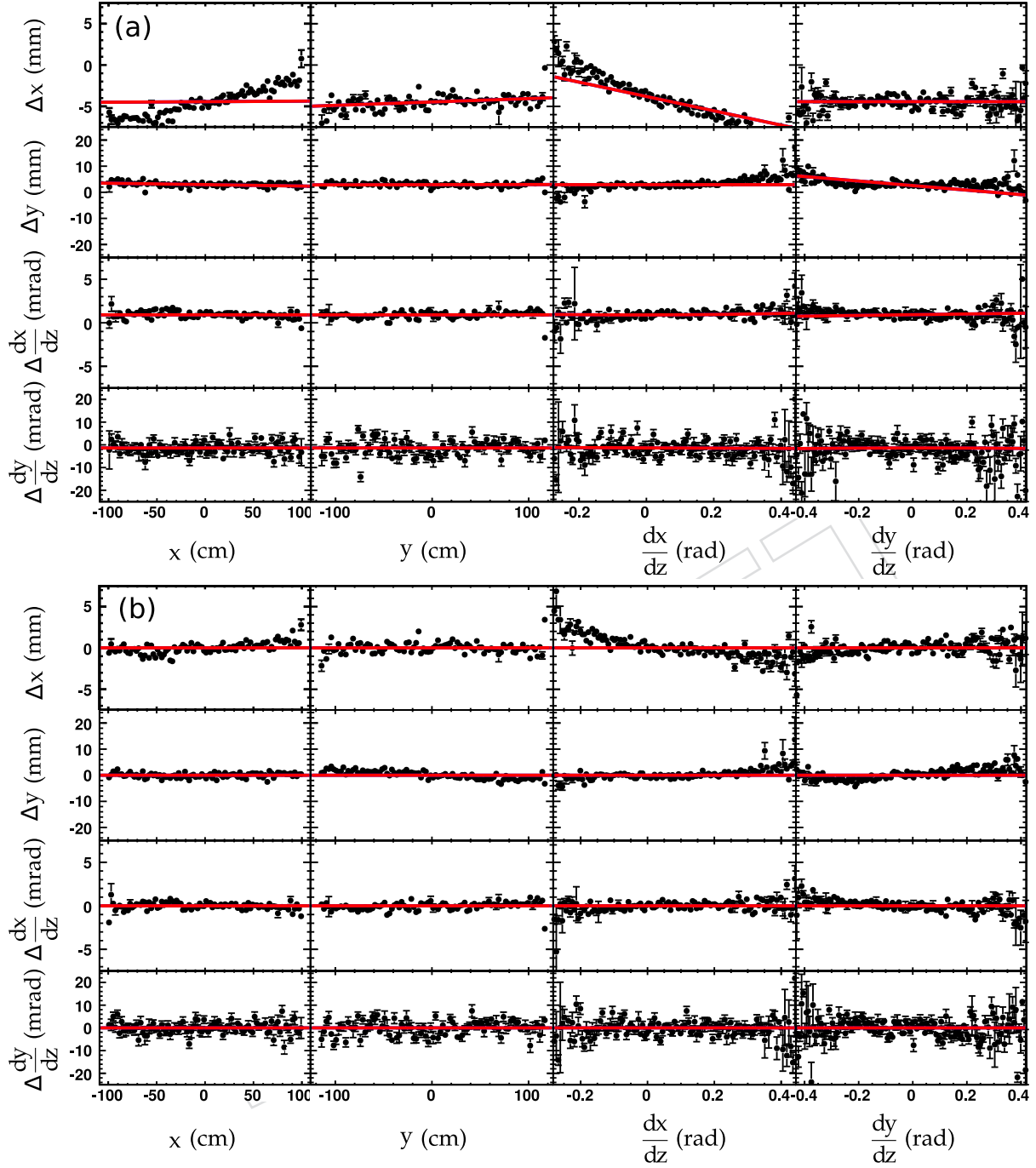
CMS 2008

Figure 6: Mean residuals with statistical error bars versus position (x, y) and entrance angle ($\frac{dx}{dz}$, $\frac{dy}{dz}$) in one chamber (DT wheel 0, station 1, sector 10) from cosmic-ray data, (a) before alignment and (b) after alignment. Each bin selects a narrow range of the position or entrance angle component under consideration, but averages over all other variables. The fit function, evaluated at zero in all other variables, is overlaid as lines before and after alignment. Asymmetries in the position and entrance angle distributions allow for misalignments to be manifested in more ways in the averaged residuals than in the projections of the best-fit function, but the fit properly removes these misalignments, resulting in nearly flat lines in all variables.

403   chambers (in wheel, station, sector $(-1, 2, 8)$, $(+1, 3, 8)$, $(-1, 1, 12)$, and $(+1, 2, 2)$) failed to
404   converge, all for reasons related to the scarcity of horizontal cosmic ray muons.

405   For most chambers within the restricted set, however, cosmic-ray muons are sufficiently abun-
406   dant that the measurement is not statistics-limited. It is therefore possible to apply a tight set
407   of track quality requirements, to control systematic errors:

408   • $100 < p_T < 200$ GeV/c (nearly straight tracks; the upper limit guarantees statistical
409   independence from one of the cross-checks);

410   • 12 out of 12 hits in DT chambers of stations 1–3, 8 out of 8 hits in DT chambers of
411   station 4;

412   • at least 15 hits on the tracker track, with $\chi^2/\mathrm{ndf} < 10$.

413   The cosmic-ray period included several on-off cycles of the magnetic field, and the full field
414   (3.8 T) periods were shown to result in reproducible alignment parameters with the hardware
415   system [3] and track residuals. Only datasets marked as acceptable for physics with full field
416   from the CMS "run registry" [4] were used. Of the 270 million cosmic-ray triggered events
417   in CRAFT, the above requirements select 100 000 tracks (the reduction is primarily due the
418   p_T selection and the requirement that cosmic-ray trajectories to pass through the tracker), yet
419   statistical uncertainties are typically only 120 μm in δ_x. Systematic errors, which may amount
420   to several hundred microns, dominate the alignment parameter uncertainties, and hence it is
421   better to select the highest-quality muons.

422   DT chambers in stations 1–3 are aligned in all six degrees of freedom, but chambers of sta-
423   tion 4 are only aligned in δ_x, δ_{ϕ_y}, and δ_{ϕ_z}, as these are the most sensitive alignment parameters
424   without Δy and $\Delta\frac{\mathrm{d}y}{\mathrm{d}z}$ residuals (recall that station 4 chambers have no y-measuring superlayer).
425   Unaligned coordinates are not allowed to float in the minimization.

5.2   Monte Carlo Study

427   To test the alignment algorithm, a large sample of cosmic rays was simulated (using CMSCGEN,
428   described in Ref. [16]), tracks were reconstructed with misaligned muon chambers (2 mm Gaus-
429   sian smearing in x, 4 mm in y and z, 2 mrad in ϕ_x, ϕ_y, and ϕ_z), and the algorithm was applied to
430   restore the original alignment parameters using only the tracks. To focus on the accuracy of the
431   algorithm itself, the tracker geometry, internal muon layer geometry, magnetic field map, and
432   material distribution were modeled without errors (identical in simulation and reconstruction).
433   All other detector effects were realistically modeled.

434   The test was performed twice, the first time with 350 000 tracks passing all selection require-
435   ments and again with 100 000 tracks (a subsample). The first can be considered an infinite-
436   statistics limit, as statistical uncertainties from MINUIT are typically 3–4 times smaller than
437   the aligned position errors (see Tables 1 and 2). The second matches the statistical precision of
438   CRAFT. Distributions of chamber position errors are presented in Fig. 7.

5.3   Alignment Results: Residuals Distribution

440   After applying the algorithm to the CRAFT cosmic-ray dataset, the four-component distribu-
441   tion of residuals is found to be centered on zero to the same degree as in the Monte Carlo
442   simulation. Figure 8 presents the residuals distribution of all aligned chambers, where the
443   alignment makes the distribution narrower and smoother. The size of the dataset is also large
444   enough to see the non-Gaussian tails in detail, and that the simulated residuals distribution
445   closely matches the real one. However, the raw residuals do not provide a sensitive probe

Table 1: Statistical uncertainties in simulation and data: uncertainties for all chambers $i = 1$ to N are summarized by presenting $\sqrt{\frac{1}{N} \sum_i \sigma_i^2}$ where σ_i is the statistical uncertainty in one of the six alignment parameters below.

sample	δ_x (mm)	δ_y (mm)	δ_z (mm)	δ_{ϕ_x} (mrad)	δ_{ϕ_y} (mrad)	δ_{ϕ_z} (mrad)
350 k simulation	0.059	0.118	0.248	0.170	0.038	0.072
100 k simulation	0.106	0.210	0.443	0.305	0.069	0.129
100 k data	0.117	0.243	0.512	0.326	0.074	0.146

Table 2: RMS of differences between aligned and true positions of chambers in Monte Carlo simulations (distributions in Fig. 7).

sample	δ_x (mm)	δ_y (mm)	δ_z (mm)	δ_{ϕ_x} (mrad)	δ_{ϕ_y} (mrad)	δ_{ϕ_z} (mrad)
350 k simulation	0.192	0.841	0.630	0.417	0.095	0.287
100 k simulation	0.209	0.889	0.836	0.497	0.148	0.303
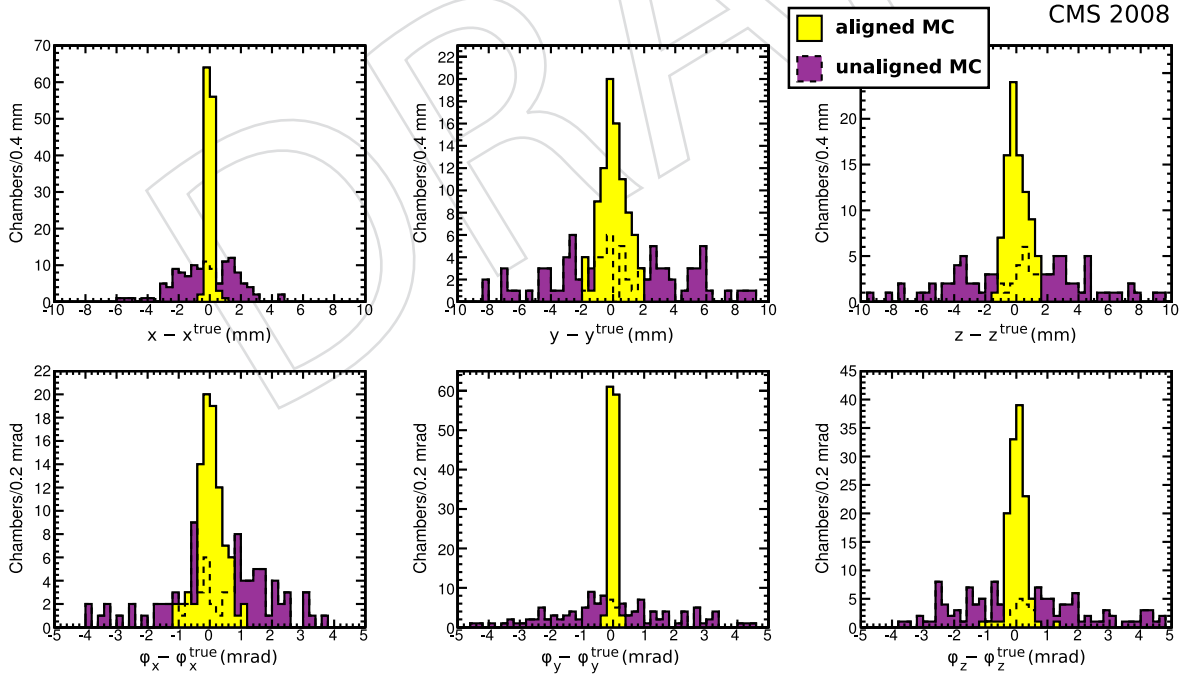
Figure 7: Differences between reconstructed and true positions of muon chambers from an alignment performed with 350 000 simulated cosmic-ray tracks passing selection requirements (only showing chambers in wheels -1, 0, $+1$, all sectors except 1 and 7).

of the alignment accuracy, because alignment corrections are typically much smaller than the width of the distribution.

For a higher sensitivity, the median of the residuals distribution of each chamber is calculated separately, then plotted as a distribution in Fig. 9, with the RMS of the distribution presented in Table 3. The median is less affected by non-Gaussian tails than the mean, and it is a different way of achieving this insensitivity than the Voigt fits used by the algorithm.

5.4 Alignment Results: Cross-check

The analysis of residuals in the previous subsection provides confidence that the alignment algorithm is operating as designed. This section presents a test of the aligned geometry using a significantly different method, namely local segment fits.

A study of alignment parameter consistency for neighboring chambers using overlapping segments from CSCs, as described in Section 4, would provide an ideal cross-check. However, most cosmic rays fall on the barrel, in which chambers do not overlap one another (with the exception of several chambers in station 4). The local alignment quality is therefore checked by comparing local segments from DT chambers in neighboring stations, propagated through only one layer of steel to the next station.

For each sector in a pair of neighboring stations (MB1→MB2, MB2→MB3, and MB3→MB4), segments are linearly propagated from the inner chamber to the outer chamber and the parameters x^{local}, $\frac{dx}{dz}^{\text{local}}$ of the propagated segment are compared with those of the segment in the outer chamber, yielding two residuals, Δx^{local}, $\Delta \frac{dx}{dz}^{\text{local}}$.

Curvature from the magnetic field is not included in this propagation, but the error is corrected by taking advantage of the fact that contributions to Δx^{local} and $\Delta \frac{dx}{dz}^{\text{local}}$ from the magnetic field are charge-dependent. Segments are associated with the corresponding tracker tracks to identify their charge and to select high transverse momentum ($p_T > 50$ GeV/c). Residuals from positively charged muons and negatively charged muons are collected separately, fitted to Gaussian distributions to identify the peaks, and averaged without weights. Since the momentum spectra of positively and negatively charged cosmic-ray muons are the same at this momentum scale, the magnetic field contributions to average Δx^{local} and $\Delta \frac{dx}{dz}^{\text{local}}$ cancel, leaving only differences from misalignments. This is the same procedure as used to test sensitivity to the magnetic field by the reference-target algorithm.

Figure 10 shows the results of these averages for each sector and pair of stations, before and after alignment, and Table 4 presents the RMS of each of the presented distributions. The distributions are convolutions of errors in the alignment and errors in the segment-matching. These results therefore only set an upper limit on the systematic uncertainties of the alignment itself. In addition, global distortions of the combined tracker and muon system are not quantified by this method. This results in an upper limit of 0.7 mm in δ_x (proportional to Δx) and 0.6 mrad in δ_{ϕ_y} (approximately proportional to $\Delta \frac{dx}{dz}$) for chambers in stations 1–3, and 1.0 mm, 0.7 mrad in station 4.

The uncertainty in point resolution along the line of sight of tracks is therefore bounded between the Monte Carlo prediction (Table 2), which includes only known propagation and detector effects, and this diagnostic, which has its own systematic uncertainties. For stations 1–3, the uncertainty is at best 200 and at worst 700 μm in δ_x.

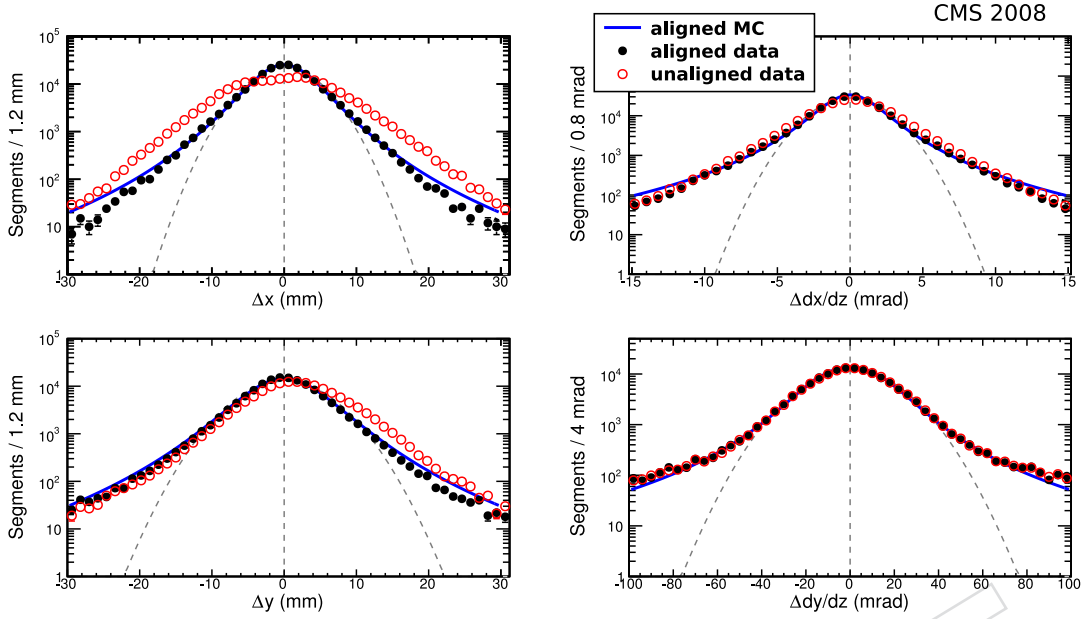Muons from proton collisions, which illuminate the endcaps, will enable a local cross-check

Figure 8: Residuals distributions before and after alignment using CRAFT data. The full curves describe the aligned Monte Carlo prediction and the light dashed curves indicate the peak of each aligned distribution and its Gaussian approximation.
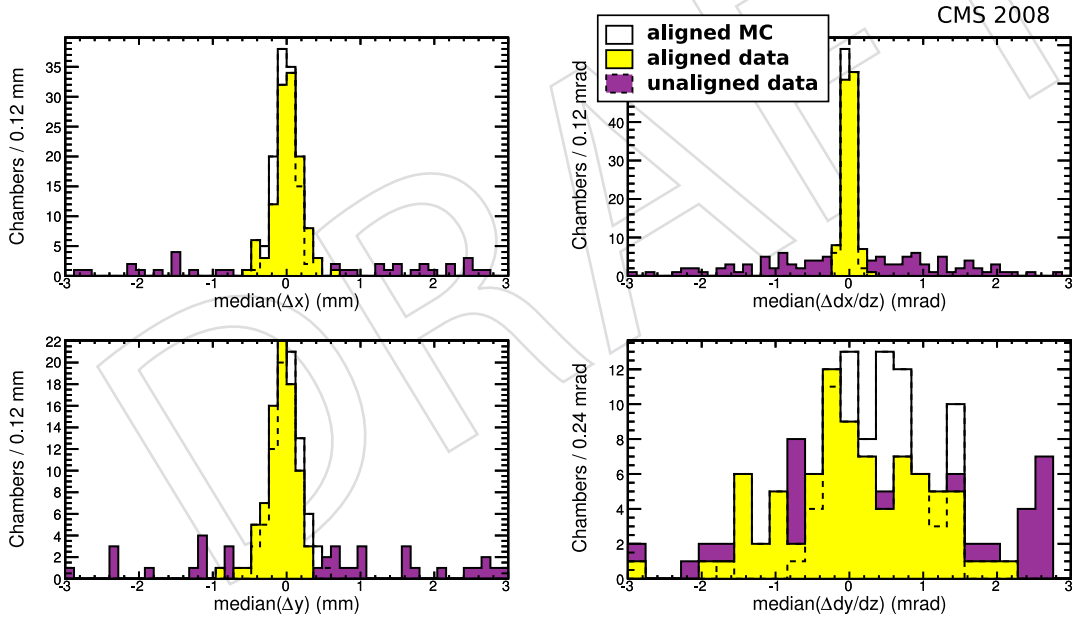

Figure 9: Medians of residuals distributions by chamber (one histogram entry per chamber).

Table 3: RMS of medians of residuals distributions by chamber (distributions in Fig. 9).

	x (mm)	y (mm)	$\frac{dx}{dz}$ (mrad)	$\frac{dy}{dz}$ (mrad)
Aligned MC (100 k)	0.159	0.172	0.066	0.630
Aligned data (100 k)	0.190	0.166	0.085	0.885
Unaligned data (100 k)	5.667	2.570	1.316	1.605
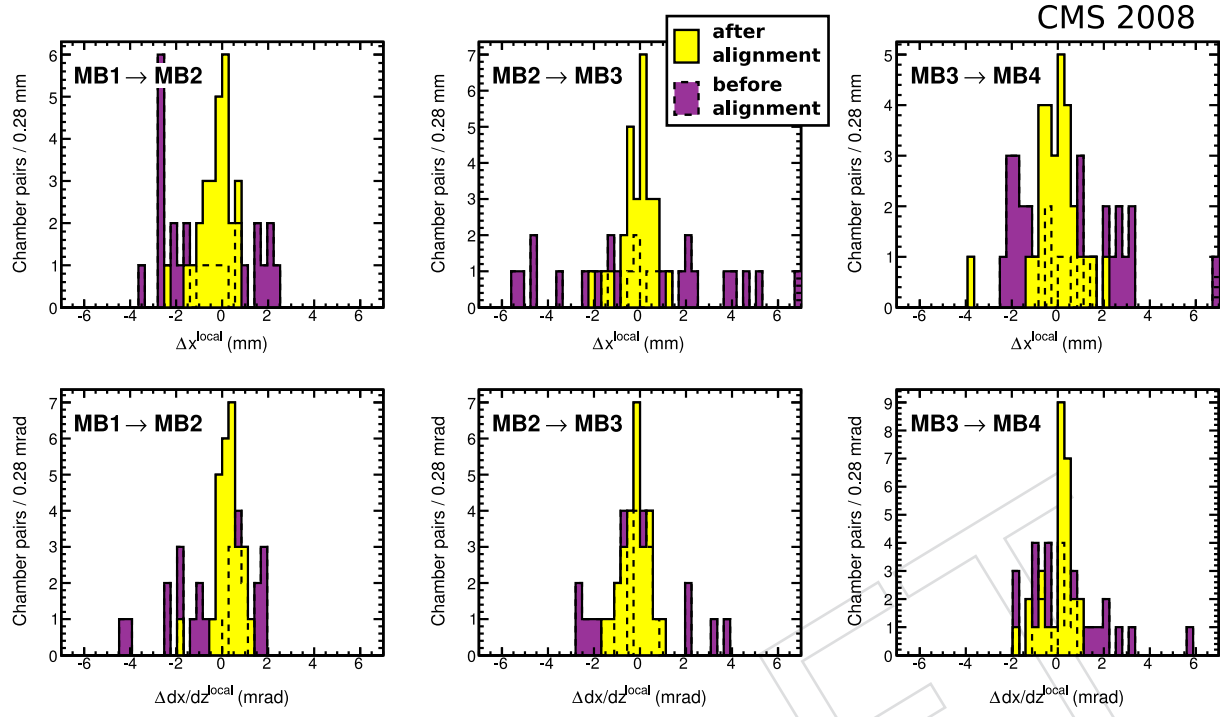
Figure 10: Differences in DT chamber positions and angles between pairs of stations as measured by locally propagated segments. Dark/dashed histograms are before alignment; light histograms are after alignment.

Table 4: RMS of pairwise position and angle differences by station (distributions in Fig. 10).

		Unaligned	Aligned
MB1 → MB2	Δx^{local} (mm)	1.82	0.68
MB1 → MB2	$\Delta \frac{\text{d}x}{\text{d}z}^{\text{local}}$ (mrad)	1.68	0.57
MB2 → MB3	Δx^{local} (mm)	3.20	0.69
MB2 → MB3	$\Delta \frac{\text{d}x}{\text{d}z}^{\text{local}}$ (mrad)	1.56	0.60
MB3 → MB4	Δx^{local} (mm)	2.17	1.06
MB3 → MB4	$\Delta \frac{\text{d}x}{\text{d}z}^{\text{local}}$ (mrad)	1.65	0.70

with the CSC ring method of Section 4. Since the latter has a demonstrated position uncertainty of 270 μm, such a comparison will considerably tighten the bound on alignment resolution uncertainty.

5.5   Alignment Results: Effect on Momentum Measurement

The motivation for the alignment effort is to correct reconstructed muon momentum distributions, so the trajectories of cosmic-ray muons are re-fitted with the new geometry to verify that the resolution has improved. For sensitivity to the effect of misalignments in the muon system, energetic cosmic rays are selected with $p_T > 200 \, \text{GeV}/c$, a sample which is independent of the $100 < p_T < 200 \, \text{GeV}/c$ tracks used to perform the alignment. Tracks are reconstructed using hits from the tracker and the first muon station, a simple way to optimize high-momentum muon resolution by increasing the effective lever arm of sagitta measurements while minimizing bias from radiative muon showers, which become prominent at several hundred GeV/c. It also focuses on the connection between the tracker and the first muon station, a pair that was not tested with the segments described in Section 5.4.

The top half and bottom half of the cosmic ray trajectory are reconstructed separately, split at the point of closest approach to the LHC beamline. Any difference in track parameters between the top and bottom fits is purely instrumental: in Fig. 11 the fractional difference in curvature $(\Delta\kappa/(\sqrt{2}\kappa) = (\kappa_{\text{top}} - \kappa_{\text{bottom}})/(\sqrt{2}\kappa)$ where $\kappa = q/p_T)$ is plotted before and after alignment; the tracker-only reconstruction is also given, for reference. Assuming that the measurements in the top and bottom parts of CMS are statistically independent with equal resolutions, this plot represents the fractional error in the curvature of tracks, which is approximately equal to the fractional error in its reciprocal, p_T. Some global distortions correlate misalignments in the top and bottom parts of the detector; this test is insensitive to such modes. The fitted resolution is given in Table 5.

The majority of muons in this study have a momentum close to the 200 GeV/c threshold because of the steeply falling distribution of cosmic rays. At 200 GeV/c, the momentum resolution of the combined system is not expected to significantly exceed the resolution of the tracker alone (see Ref. [17], Fig. 1.5), but the biased distribution prior to alignment has been repaired by alignment procedure.

5.6   The Millepede Algorithm

A Millepede algorithm [7] is under development to align the muon chambers relative to the tracker, as an alternative to the reference-target algorithm. Instead of using a general non-linear fitting package to minimize the objective function, Millepede linearizes the problem and solves it with matrix inversion. A potential application of this method is to combine in a single fit measurements from tracker tracks and the locally fitted segments described in Section 5.4, thereby optimizing statistical precision. Before such a generalization is used, however, it must be tuned to reproduce the results of the reference-target algorithm. When configured to use tracker tracks only, the objective function is

$$\chi^2 = \sum_i^{\text{chambers}} \sum_i^{\text{tracks}} \left(\Delta\vec{x}_j - A_j \cdot \vec{\delta}_i \right)^T (\sigma_{\text{residual}}{}^2)_{ij}^{-1} \left(\Delta\vec{x}_j - A_j \cdot \vec{\delta}_i \right) \quad , \tag{10}$$

where $\Delta\vec{x} = (\Delta x, \Delta y, \Delta\frac{\mathrm{d}x}{\mathrm{d}z}, \Delta\frac{\mathrm{d}y}{\mathrm{d}z})$, A_j is the matrix in Eq. (7), and $(\sigma_{\text{residual}}{}^2)_{ij}^{-1}$ is the inverse of the residuals covariance matrix.

To avoid the influence of non-Gaussian tails, noisy channels, and pattern-recognition errors in the determination of the peak of the residuals distribution, large residuals were excluded,
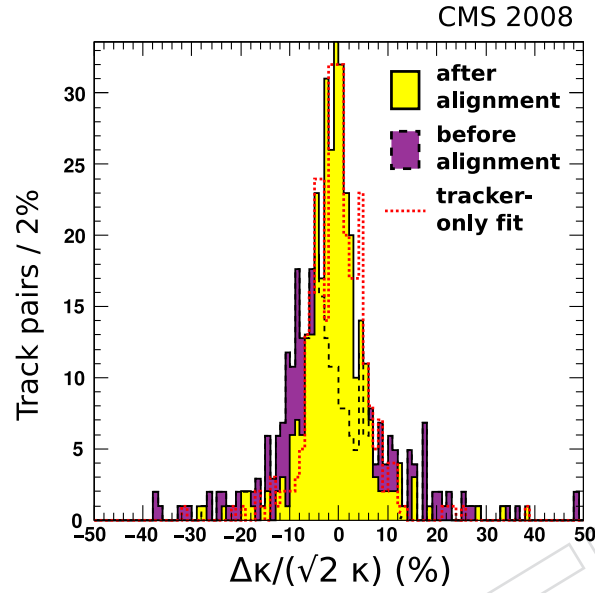
Figure 11: Fractional curvature difference between the top and bottom parts of CMS for muons with $p_T > 200 \, \text{GeV}/c$ ($\kappa = q/p_T$). Dark/dashed distribution is before alignment, light is after alignment (using the reference-target algorithm), and the open dotted distribution is tracker-only.

Table 5: RMS and Gaussian core fits of the fractional curvature distributions in Fig. 11. The fits include all data in the central region $\left| \Delta\kappa/(\sqrt{2}\kappa) \right| < 2 \times \text{RMS}$.

	Gaussian mean (%)	Gaussian width (%)	RMS (%)
Unaligned	-2.5 ± 0.6	8.6 ± 0.5	12.3
Aligned	-0.9 ± 0.3	4.3 ± 0.2	6.9
Tracker-only	0.3 ± 0.3	4.5 ± 0.2	6.4

Table 6: Accuracy of Millepede alignment in Monte Carlo simulations (350 k tracks), varying the selection threshold of the excluded region. The resolution attained with a threshold of $2.5\,\gamma$ reproduces that of the reference-target algorithm presented in Table 2.

selection threshold	δ_x (mm)	δ_y (mm)	δ_z (mm)
$1.0\,\gamma$	0.41	1.05	2.39
$1.5\,\gamma$	0.30	0.89	1.46
$2.0\,\gamma$	0.26	0.84	0.92
$2.5\,\gamma$	0.25	0.84	0.78
$3.0\,\gamma$	0.25	0.85	0.78

symmetrically around the peak, for each of the four residuals components. Threshold values for the excluded region are derived from Cauchy-Lorentzian fits. With x_0 and γ being the mean and half-width at half maximum, only residuals between $x_0 - 2.5\,\gamma$ and $x_0 + 2.5\,\gamma$ enter the sum in Eq. (10) for all four components. The optimum threshold was chosen from the study presented in Table 6, which lists alignment position accuracy as a function of the threshold value.

6   Summary and Discussion

This paper has presented a variety of procedures to align different parts of the muon system with tracks: layers in DT chambers, CSC chambers in rings, and DT chambers in a coordinate frame shared with the tracker. The available data have been fully exploited: horizontal beam-halo and vertical cosmic-ray muons. Through comparisons with independent data, it was shown that the superlayer $r\phi$ resolution is 80 μm within each DT chamber, that the $r\phi$ resolution of CSC chambers is 270 μm within each endcap ring, and that the DT chamber positions along the tracks are known with an accuracy between 200 and 700 μm (stations 1–3, wheels -1, 0, $+1$).

In addition, several new techniques have been introduced. The superlayer structure of DT chambers permits an analysis of layer geometry in a way that uses tracks alone, and therefore rigorously compares the result obtained with tracks with the results from survey measurements. The overlap of CSC rings permits an analytic solution to its alignment. Non-Gaussianity in the physics of track propagation through the steel yoke implies a non-linear extension to the general alignment method.

Techniques which will be useful for re-aligning the muon system with early LHC data have been tested. The favorable distribution of muons from collisions will broaden the applicability of these methods and open new opportunities for cross-checks and diagnostics, which ultimately will lead to a better-understood momentum resolution for high-momentum muons and increased discovery reach for high-energy processes.

Acknowledgements

References

[1] CMS Collaboration, "The CMS experiment at the CERN LHC", *JINST* **3** (2008) S08004.
`doi:10.1088/1748-0221/3/08/S08004`.

[2] L. Evans and P. Bryant, (eds.), "LHC Machine", *JINST* **3** (2008) S08001.
`doi:10.1088/1748-0221/3/08/S08001`.

[3] CMS Collaboration, "Aligning the CMS Muon Chambers with the Muon Alignment
System during the Cosmic Run of 2008", *submitted to JINST* (2009).

[4] CMS Collaboration, "Commissioning of the CMS Experiment and the Cosmic Run at
Four Tesla", *submitted to JINST* (2009).

[5] CMS Collaboration, "From Detector to Analysis: CMS Data Processing Workflows
During an Extended Cosmic Ray Run", *submitted to JINST* (2009).

[6] CMS Collaboration, "Performance of the CMS Cathode Strip Chambers with Cosmic
Rays", *submitted to JINST* (2009).

[7] V. Blobel, "Software alignment for tracking detectors", *Nucl. Instrum. Meth.* **A566** (2006)
5–13. `doi:10.1016/j.nima.2006.05.157`.

[8] V. Drollinger, "Simulation of Beam Halo and Cosmic Muons", *CMS Note* **2005/012** (2005).
`http://cms-secr.web.cern.ch/cms-secr/documents/05/note05_012.pdf`.

[9] R. Goudard, J. F. Fuchs, and J. D. Maillefaud, "Photogrammetry of the YE−2 Face Z−
ME−3 Layer CERN SX5". `https://edms.cern.ch/document/866869/1`.

[10] V. Karimaki, A. Heikkinen, T. Lampen, and T. Linden, "Sensor alignment by tracks", *In
the Proceedings of 2003 Conference for Computing in High-Energy and Nuclear Physics
(CHEP 03), La Jolla, California, 24-28 Mar 2003, pp TULT008* (2003)
`arXiv:physics/0306034`.

[11] CMS Collaboration, "Alignment of the CMS Silicon Tracker during Commissioning with
Cosmic Rays", *submitted to JINST* (2009) `arXiv:0910.2505`.

[12] F. James and M. Roos, "Minuit: A System for Function Minimization and Analysis of the
Parameter Errors and Correlations", *Comput. Phys. Commun.* **10** (1975) 343–367.
`doi:10.1016/0010-4655(75)90039-9`.

591 [13] CMS Collaboration, "Precise Mapping of the Magnetic Field in the CMS Barrel Yoke
592   using Cosmic Rays", *submitted to JINST* (2009).

593 [14] G. Flucke, P. Schleper, G. Steinbruck, and M. Stoye, "CMS silicon tracker alignment
594   strategy with the Millepede II algorithm", *JINST* **3** (2008) P09002.
595   `doi:10.1088/1748-0221/3/09/P09002`.

596 [15] M. Stoye and P. Schleper (dir.), "Calibration and Alignment of the CMS Silicon Tracking
597   Detector". PhD thesis, Univ. Hamburg, Hamburg, 2007.
598   `http://cdsweb.cern.ch/record/1047047`.

599 [16] P. Biallass and T. Hebbeker, "Parametrization of the Cosmic Muon Flux for the Generator
600   CMSCGEN", `arXiv:0907.5514`.

601 [17] CMS Collaboration, "CMS technical design report, volume II: Physics performance",
602   *J. Phys.* **G34** (2007) 995–1579. `doi:10.1088/0954-3899/34/6/S01`.